CrossMark

ORIGINAL ARTICLE

Dominant factor analysis of B-flow twinkling sign with phantom and simulation data

Weijia Lu[1] · Bruno Haider[2]

Abstract

Background and purpose The twinkling sign in B-flow imaging (BFI-TS) has been reported in the literature to increase both specificity and sensitivity compared to the traditional gray-scale imaging. Unfortunately, there has been no conclusive study on the mechanism of this effect.
Methods In the study presented here, a comparative test on phantoms is introduced, where the variance of a phase estimator is used to quantify the motion amplitude. The statistical inference is employed later to find the dominate factor for the twinkling sign, which is proven by computer simulation.
Results Through the analysis, it is confirmed that the tissue viscoelasticity is closely coupled with the twinkling sign. Moreover, the acoustic radiation force caused by tissue attenuation is found to be the trigger of the twinkling sign.
Conclusion Based on these findings, the BFI-TS is interpreted as a tissue movement triggering vibration of microcalcifications particle.

Keywords B-flow image · Twinkling sign · Microcalcification

✉ Weijia Lu
  AlfredWJLu@gmail.com

1 GE Global Research, Shanghai, China

2 GE Healthcare, Ultrasound Probes, Phoenix, AZ, USA

Introduction

Microcalcifications (MC) are small crystals of calcium apatites in the human tissue [1]; their number, size, morphology, and distribution are said to be important indicators in the diagnosis of cancer. For instance, a large number of MCs are predictive for an increased risk of invasion in ductal carcinoma *in situ* (DCIS) [2], and those located within a thyroid nodule indicate a higher likelihood of thyroid malignancy [3]. Studies performed to understand the ability of ultrasound to detect MCs date back to the 1990s by Anderson and his colleagues [1, 4–6]. These studies primarily evaluated MC detection using gray-scale US. Later, after B-flow imaging (BFI) was introduced in 2000 by GE Medical System [7], it was also applied to the MC detection problem. An interesting phenomenon called B-flow imaging twinkling sign (BFI-TS) was reported in 2008 [8, 9]. With it as a diagnosis factor, an increase in specificity and sensitivity of 5 % and 39 %, respectively, was reported as compared with the traditional gray-scale imaging for the diagnosis of papillary thyroid cancer (PTC). To further reveal the mechanism of this phenomenon, a soft-tissue-mimicking phantom with embedded glass beads was used by Liu et al. [10]. A high-speed optical system to capture the scattered light and a post-analysis of these signals showed a tight correlation between the occurrence of twinkling and the oscillation of the glass beads under radiation force [10]. However, so far, the simulation of the twinkling sign in B-flow mode still lacks results; it is hoped that such results could bring flexibility and additional understanding to this phenomenon [10]. Meanwhile, a systematically designed experiment to help explore the underlying mechanism is absent in the literature. The terminology of the twinkling sign (TS) itself was first introduced by Rahmouni [11] in color Doppler mode.

Springer

Several hypotheses for its origin were proposed after that; the three major ones are the roughness of scatter surface [11], phase jitter [12], and micro-oscillation [13]. Although these hypotheses are mainly for the TS in color flow imaging (CFI), they likely could be the potential source in BFI, and serve as the starting point to interpret BFI-TS.

Addressing the aforementioned opportunities for the current BFI-TS research, this study is presented. In the first part of this paper, factorially designed phantom experiments are used for the verification and further exploration of the mechanism of BFI-TS. In these experiments, B-flow images and in-phase quadrature (IQ) signals for a number of setups are captured. The setups include (a) MCs of different sizes in a homogeneous breast-tissue-mimicking background and (b) MCs in two phantoms with homogeneous background and carefully controlled viscoelasticity. After that, based on the work of Liu and the observation in the phantom experiment [10], the mechanism of BFI-TS is discussed in terms of computational simulation. First, a theoretical model for simulations is established and implemented with the FIELD II [14] and the COMSOL Multiphysics (COMSOL Inc.). This model simulates the acoustic field generated by a linear transducer and the coherent scattering from an MC. Thereafter, the interaction between the MC and the acoustic field is also evaluated by taken acoustic radiation force, from scattering as well as the attenuation, as the driving force in another mechanical simulation. Finally, the BFI rational frequency (RF) signals are composed

from the motion of the MC. The whole simulation procedure is built by following the micro-oscillation hypothesis [13], since (a) the oscillation of scattered light from smooth glass beads under radiation force was observed before [10] and (b) phase jitter errors are largely eliminated in modern ultrasound systems.

Materials and methods

Recalling generation of the BFI and the notation in this study

BFI is the image obtained in the B-flow tissue scanning mode. Without losing the generality, the BFI refers interchangeably to the image or the related scanning mode in this study. Compared with common B-mode images, the beam is scanned in an interleaved way in B-flow tissue mode [15] (Fig. 1), and the transmit wave to the tissue is coded by several bits of binary code (barker code). As the interleaved scanning takes place iteratively four times to the same position shown in the Fig. 1, four B-mode IQ frames are generated after the assembling of the decoded backscattering IQ signal. The final BFI IQ frame is then calculated based on these B-mode frames through a high-pass digital filter, normally called the coherent filter. The details of the coding/decoding strategy, i.e., the pulse compression, in a BFI are available in two previous studies [7, 16]. In the present study, the method introduced later is


Fig. 1 Example of interleaved scanning setup and coherent filtering for BFI. Two scanning groups, whose sizes equal the 'sensitivity' parameter on the US panel (five in this example), are repeated four times at each position.
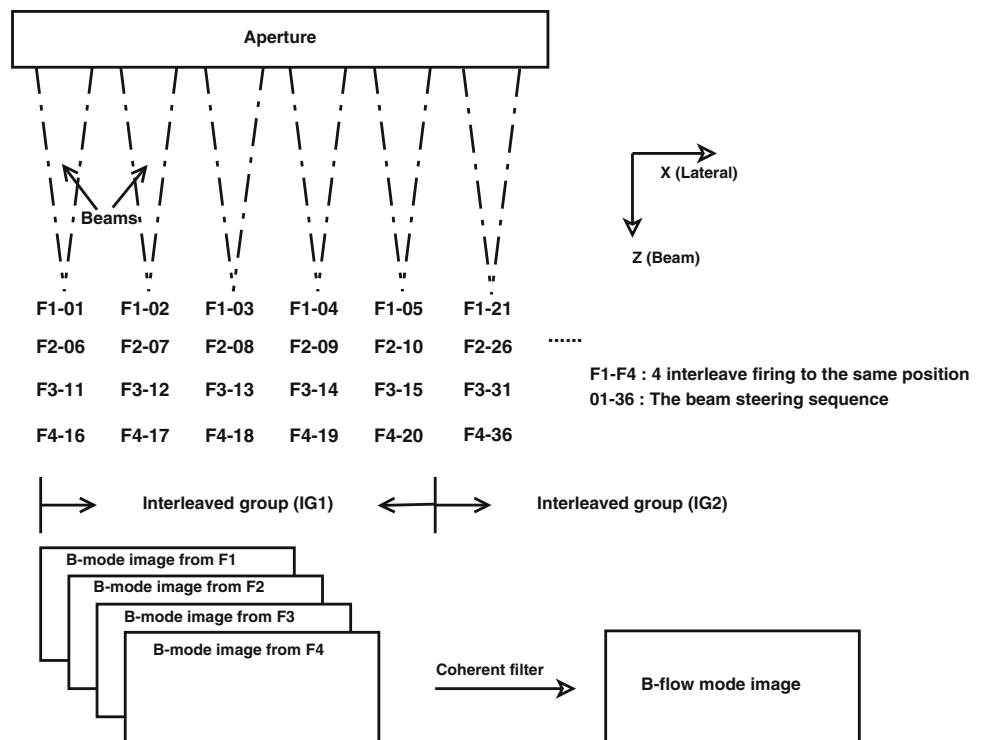
Table 1 List of symbols in this paper

f0	Central frequency of the transmission
F#	F number, the focal depth over the diameter of the aperture
φ_{cc}	The phase estimator for estimation of the movement between ensemble fires
ω_L	The nature frequency of a harmonic vibration
ζ_m	The amplitude of a harmonic vibration
$\mathbf{F_0}$	The primary acoustic force exerted on the particle
F_1	The acoustic force coming from the attenuation of the tissues
S_0	The close surface around particle, to estimate the $\mathbf{F_0}$
$\mathbf{n}$	The external unit normal vector of a surface
T	The Lagrange density
p_t	The total pressure field, or the summation of the incident field and scattering field
p_{sc}	The scattering field
$\mathbf{v}$	The local velocity in a pressure field
c	Sound speed or the interchangeable longitudinal wave velocity
c_c	The complex sound speed caused by the dispersive tissue
I	Sound level of the acoustic field
α	The attenuation coefficient of the tissue
ω	The angular frequency of the transmission
ρ	The density
ρ_c	The complex density caused by the dispersive tissue
μ	Dynamic viscosity
μ_B	Bulk viscosity
S_d	The stress tensor
ε_d	The deviatoric elastic strain
G	Shear modulus
η	The viscosity of the Kelvin–Voigt material

Fig. 2 Example of generating color-coded expression. Two IQ complex waves related to the same spatial region of interest (*gray rectangle*) are cross-correlated by Eq. 1, and the estimated φ_{cc} values are then projected to color space to generate a color-coded expression. The *dotted lines* and *circle* in this figure show the sequence of actions.
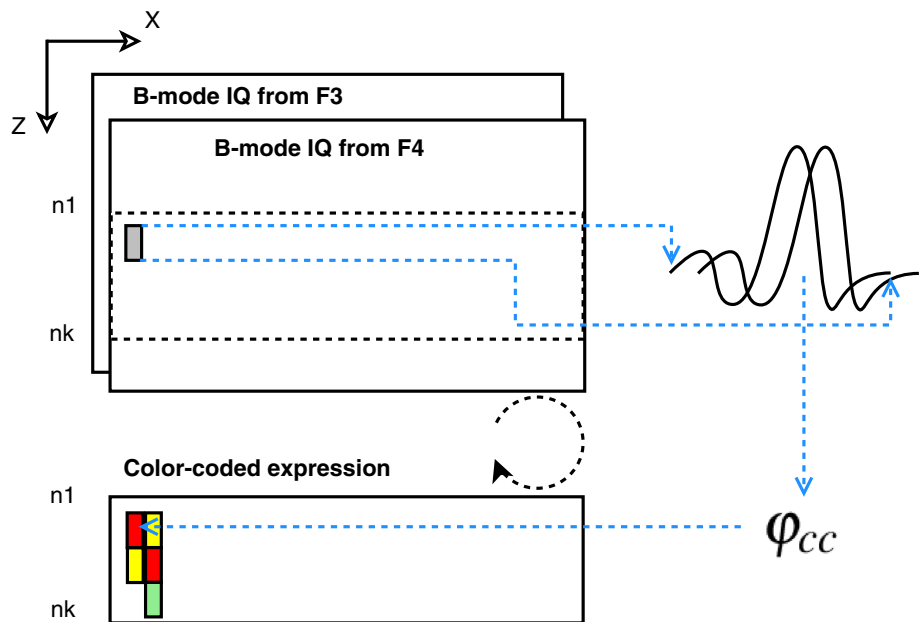
Table 2 Acoustic parameters of homogeneous phantom with viscoelasticity controlling

Type	C (m/s)	Attenuation [dB/(cm MHz)]	Mechanic modulus/dissipation factor	
			Bulk modulus (MPa)	Shear modulus (KPa)
Hard	1551	0.080	2.4/0.046	58/0.090
Soft	1548	0.032	2.4/0.016	3.6/0.060

built on the interpretation of the procedure to generate a BFI image. For the consistency and the efficiency of the representation, the notation is first given in Table 1.

Exploring the dominant factor for the twinkling sign

In the factorially designed phantom experiment to reveal the dominant factor for BFI-TS, an LE9 US machine and ML6-15 probe (General Electric Co.) are used to capture BFI IQ data. The location of the MC is marked by μCT (Vltomelx S, General Electric Co.) before the experiment. During the experiment, a single emission focal zone is set close to the MC target, and the scanner parameters are optimized to get the best observation in B-mode before switching to B-flow tissue mode to capture image and IQ data (the common ultrasound settings in BFI during the following phantom experiments are minimal line density, maximal power output, flow type high, background turned on, maximal frame average, no suppression in noise and flash, sensitivity 50, f0 = 5 MHz, F# 4). During the experiment, the parameters, such as transmitter/receiver control, scanning time sequence, geometry pattern, and those for signal processing, are also recorded along with IQ data. In addition, during the scanning, the probe is always clamped, and gel is used for acoustic coupling between probe and phantom.

In the analysis, the cross correlation is introduced to generate a phase estimator φ_{cc} from the ensemble IQs ($k = 1, \ldots 4$ iteratively firing from the same interleaved scanning group) [17–19]. The details of calculation, as could be found in Marple's contribution [19], are reprinted as follows due to its importance to this study: first, the maximum peak in the cross-correlation trace $CC_{(k,k+1)}(t)$ is found, i.e., the moment when $t = \Delta t$ in Eq. 1 (the derivation of this equation is in the "Appendix"). At this point, the phase of the complex cross correlation is determined only by the center frequency and time lag on the ensemble signal (say caused by motion), as seen in the highlighted part of Eq. 1.

From this phase, denoted by φ_{cc}, the movement between firings can be estimated, and further aggregated in the image plane to generate a graphic representation (as shown in Fig. 2). Without exception, this kind of representation is called color-coded expression in the following sections:

$$
\begin{aligned}
CC_{(k,k+1)}(t) &= |CC_{(k,k+1)}(t)| \cdot e^{j\phi_{CC(k,k+1)}(t)} \\
&= |CC_{(k,k)}(t - \Delta t)| \cdot e^{j(\phi_{CC(k,k)}(t-\Delta t) - \underline{\omega_0 \Delta t})}.
\end{aligned} \tag{1}
$$

Moreover, as deduced in the Appendix, the variance of phase estimator φ_{cc} could quantify the motion of vibration, as reprinted in Eq. 2:

$$
\sigma_{\varphi_{cc}}^2 = \frac{4}{c^2}(\zeta_m \omega_0)^2 (1 - \cos(\omega_L \Delta T)). \tag{2}
$$

From this equation, it is found that the variance of the φ_{cc} is governed by two parameters: ω_L and ζ_m. If ω_L (the natural vibration frequency) approaches zero, or ζ_m (the vibration amplitude) becomes small, the variance of the phase estimator should become smaller. Thus, the variance of φ_{cc} around MC (≈ 0.9 mm in range) can be used to make statistical inference.

In the statistical interference, the unbiased standard deviation with Bessel's correction is used as the point estimator of the standard deviation of φ_{cc}. In addition, the calculation is on the small chunk divided from the observations. Later on, traditionally, a linear model is easily introduced, with the interested factor as the explanatory variables and the unbiased standard deviations as the target. Based on this linear model, the p value derived from the hypothesis test on each coefficient can indicate the dominant factor for the twinkling sign.

Phantoms for factorial experiment

The following phantoms are used in the experiment:

A. One homogeneous tissue-mimicking (TM) phantom with variation in particle size.
B. Two homogeneous tissue-mimicking (TM) phantoms with variation in viscosity and particle size.

These phantoms, made by the authors of several Chinese national standards [20, 21], use plant-based composites to mimic the tissue background for its transparency and similar acoustic characteristics. A different size of sand as the major inclusion is placed on the congealed base, and then anchored by another layer of liquid, to represent the MC in the breast tissue. A pair of transducers to transmit and receive burst pulses is used to measure the sound speed (C) and the attenuation coefficient [20], e.g., those values printed in Table 2 measured from phantom B. Later on, the mechanical modulus and the dissipation factors can be

calculated from these two values, by Eqs. c4 and c5 in the national standard [21], or Eqs. 2.1.10 and 2.1.11 in the ultrasonic handbook [22].

Phantom A has five clusters of MC with different diameters (100, 200, 300–400, 500–600, and 800–1000 μm). The sound speed (1540 ± 10 m/s at 23 °C), attenuation (0.7 ± 0.05 dB/cm/MHz at 23 °C), and backscatter (−56 to −62 dB according to a reference equal to 2 × 10⁻²/m/sr at the measurement frequency equal to 3.5–5 MHz) are all compatible with those of tissue.

Phantom B has carefully controlled acoustic characteristics (see details in Table 2) and five MCs with various diameters embedded (0.2 mm × 2, 0.5, 1, 2 mm).

## Validation of the dominant factor by simulation

As early as the 1930s, the physical mechanism leading to the acoustic radiation force (ARF) on a sphere was reported by King [23]. Since then, ARF is more and more prevalent as a major total force in manipulating the particles in the acoustic field, and theoretical modeling is heavily studied [24–28]. The acoustic force given by the previous studies is called primary acoustic force $\mathbf{F_0}$ [29]. On the other hand, the ARF caused by tissue attenuation is widely used in ultrasonic palpation as the body force [30, 31], and it is notated as F_1 in this study. Following the steps of these great achievements, these two ARFs are considered as the driving force in the simulation based on the finite-element method (FEM). The $\mathbf{F_0}$, as the total force [N] coming from the scattering, can be expressed as an integration on a close surface S_0 around a particle [25, 27]:

$$
\mathbf{F_0} = \int_{S_0} \mathrm{d}S\langle T\rangle - \int_{S_0} \mathrm{d}S\langle \rho\mathbf{v}(\mathbf{v}\cdot\mathbf{n})\rangle,
$$

$$
T = \frac{1}{2}\rho\mathbf{v}^2 - \frac{1}{2\rho c^2}p_t^2
\tag{3}
$$

where $\langle\cdot\rangle$ denotes the average over the pulse repetition interval (PRI), $\mathbf{n}$ is the external unit normal vector for S_0, and T is the Lagrange density. In the calculation of the Lagrange density, p_t is the total pressure variation of the coherent field, namely, the first order of perturbation of the
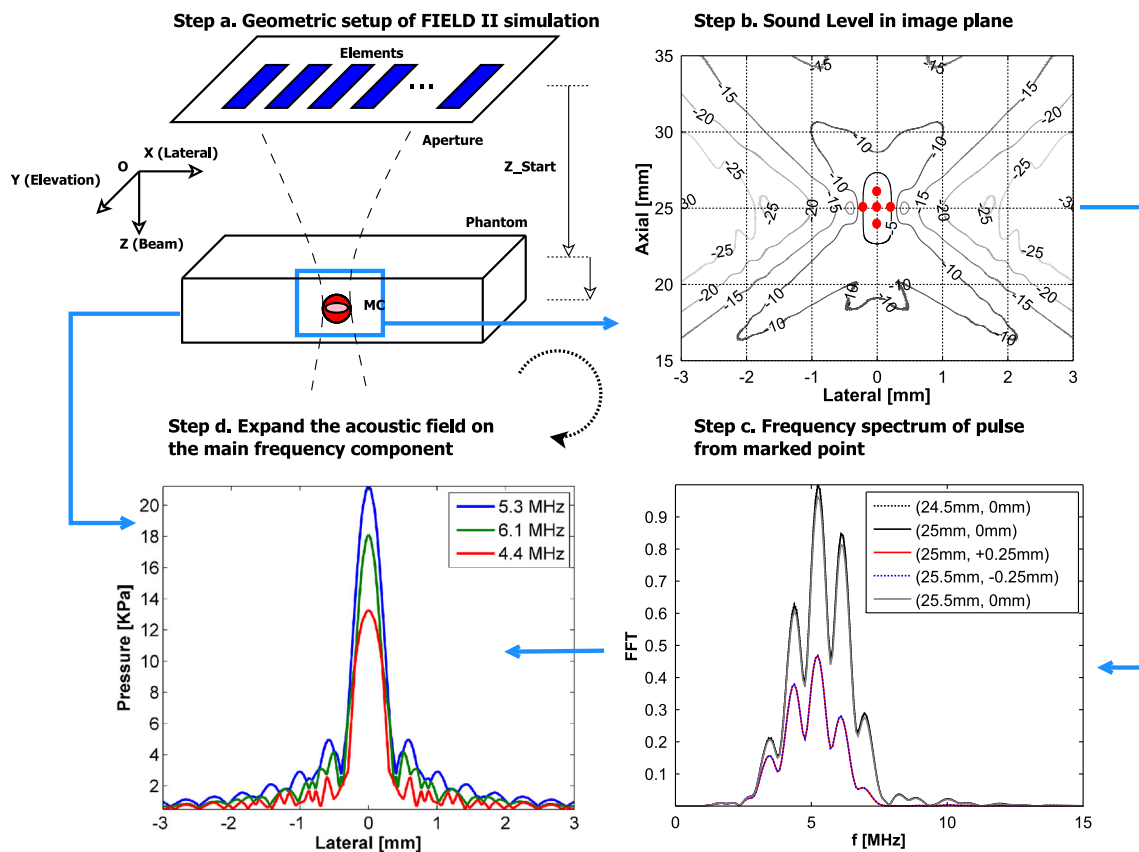
Fig. 3 Plane wave decomposition: **a** setup of simulation geometry (z_start = 20 mm, phantom height = 10 mm); **b** beam pattern estimation with FIELD II considering both attenuation and probe characteristics (geometry, transfer function, and element size), distance between aperture and MC is 25 mm; **c** spectral decomposition of pulses around MC (*red dots*); **d** plane wave decomposition of beam in focal zone around MC

pressure field when linear approximation of acoustic propagation is only taken into consideration and **v** is the local velocity.

On the other hand, F_1 in the form of the body force [kg/s^2 cm^2] from the attenuation of tissue can be expressed as in [30]:

$$F_1 = \frac{2\alpha I}{c} \tag{4}$$

where α [Np/m] is the attenuation coefficient, I [W/cm^2] is the sound level of the transmitted field, and c [m/s] is the sound speed.

To be more specific for the method in the simulation, the incident acoustic field in a certain steering location is first estimated by FIELD II [14], and decomposed into a summation of the plane waves with several major frequencies (Fig. 3) in MATLAB (MathWorks Inc.). The scattering field is then calculated in the FEM model designed by

COMSOL Multiphysics, holding two boundary conditions: the continuity of the normal components of the local velocity **v** and stress across the particle surface. Later on, the lumped acoustic field p_t is used to calculate the $\mathbf{F_0}$ operating on the MC body (Eq. 3). Meanwhile, F_1 as the body force on the whole simulation domain is estimated too (Eq. 4), together with the $\mathbf{F_0}$ to form the driving force in the kinematic model in COMSOL Multiphysics. Such a calculation is constituted step by step along with the steering of the beam in an interleave way (Fig. 1), and thus, the mimic kinematic motion generated by the LE9 US machine and ML6-15 probe can be approximated.

This estimated motion is fed back to FIELD II to calculate the backscattering RF signal. During RF calculation, the MC is modeled as a set of solids evenly distributed in the resolution cells, while the tissue is expressed by the fully developed speckle (>10 randomly distributed solids with smaller reflection coefficient in a resolution cell). The
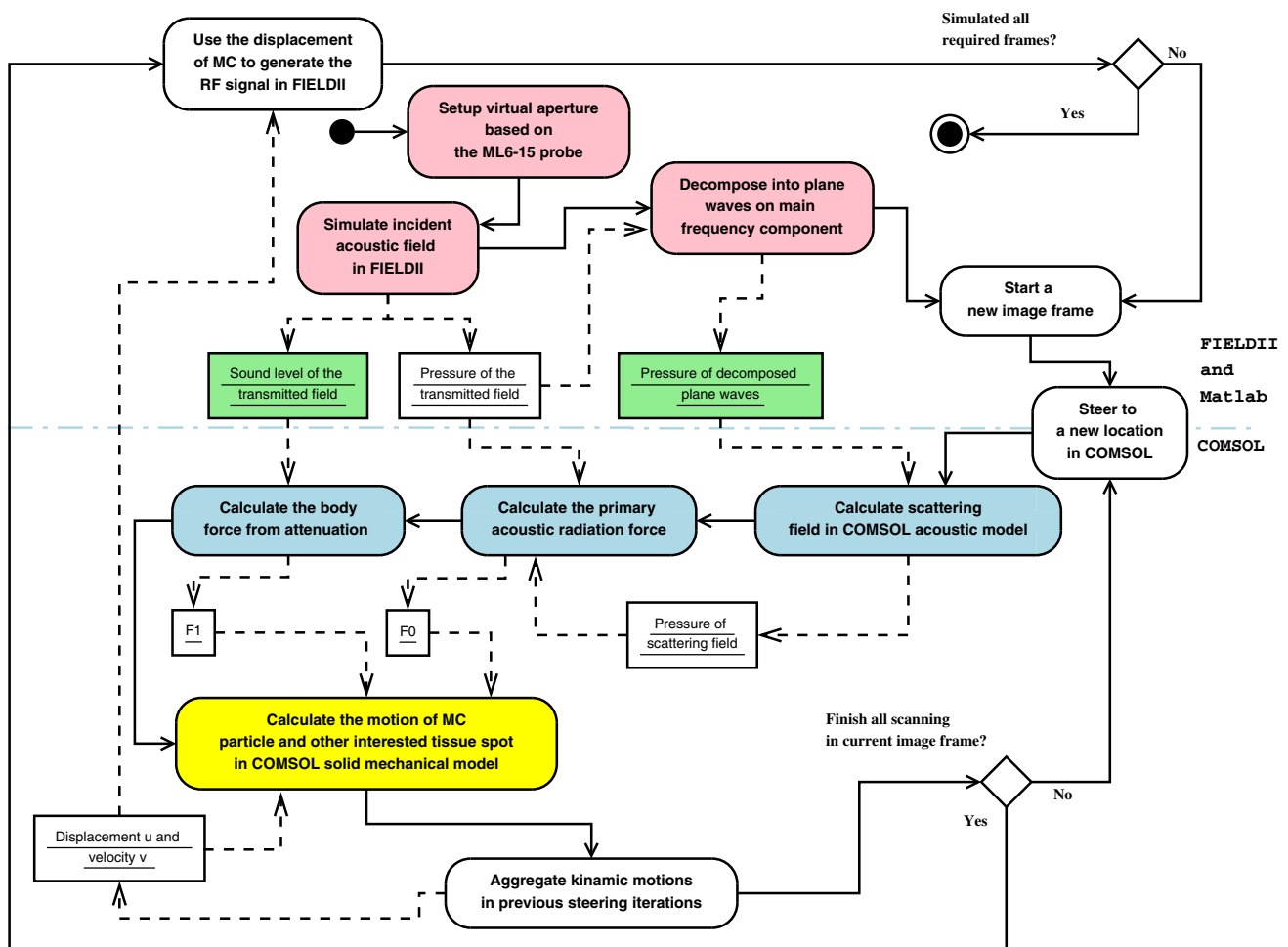
Fig. 4 Flow diagram of BFI simulation. *Solid lines* connect computational actions, and *dotted lines* show data flow. The *black circle* represents the beginning of a simulation, and its *encircled counterpart* indicates the end. *Actions above the blue-dashed line are* accomplished in FIELD II, while those below are conducted in COMSOL. Actions in *red* are the same as in the introduction in Fig. 3, and data in *green* refer to those images shown in steps **b** and **d**, respectively. In a numerical computation in COMSOL, those in *blue* represent pressure acoustics, while *yellow* ones represent solid mechanics computations
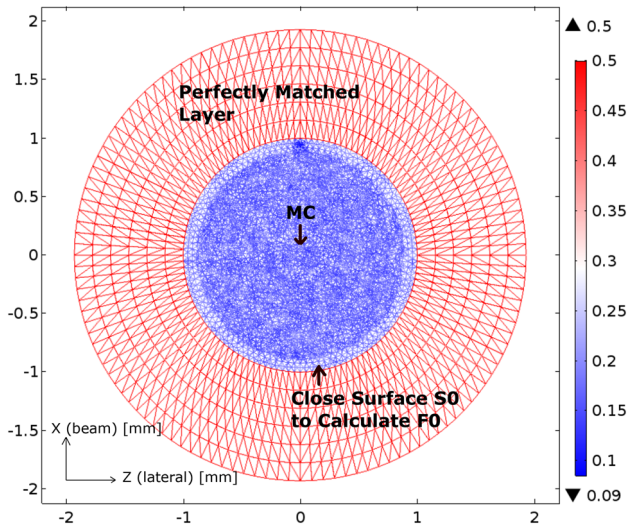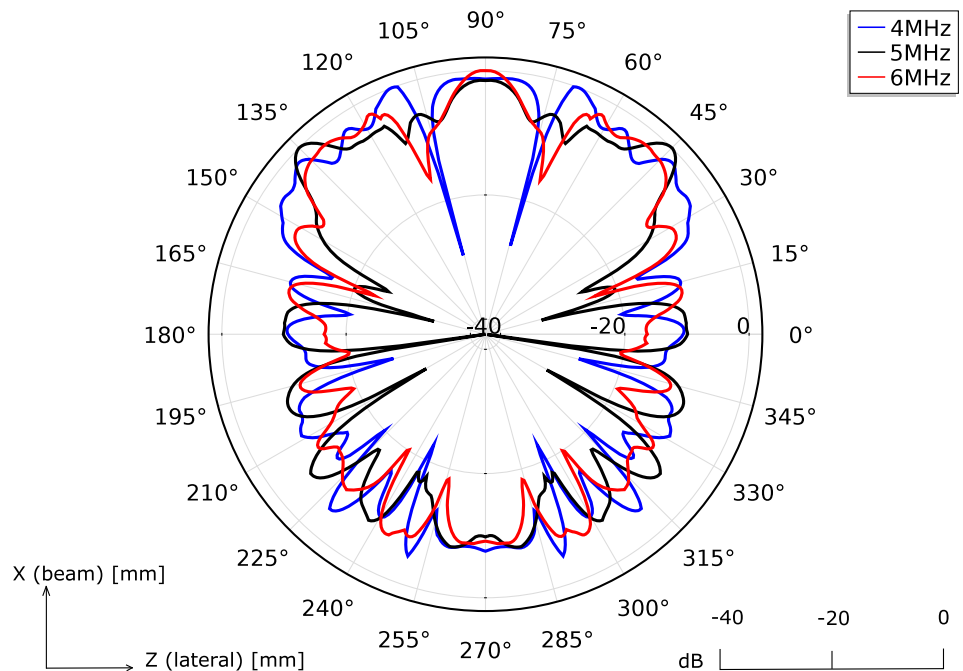
Fig. 5 Discrete mesh for pressure acoustics computation in COMSOL (*blue blocks* in Fig. 4). The *color bar* indicates normalized tetrahedron edge size over one-sixth of wavelength

RF signal then goes through compression (i.e., decoding) with a matched filter [16] and coherent filtering with a 4-tap FIR filter to finally generate the BFI signal. The aforementioned simulation procedure is graphically depicted in Fig. 4.

Geometry, mesh, materials, and governing equation for numerical modeling in COMSOL

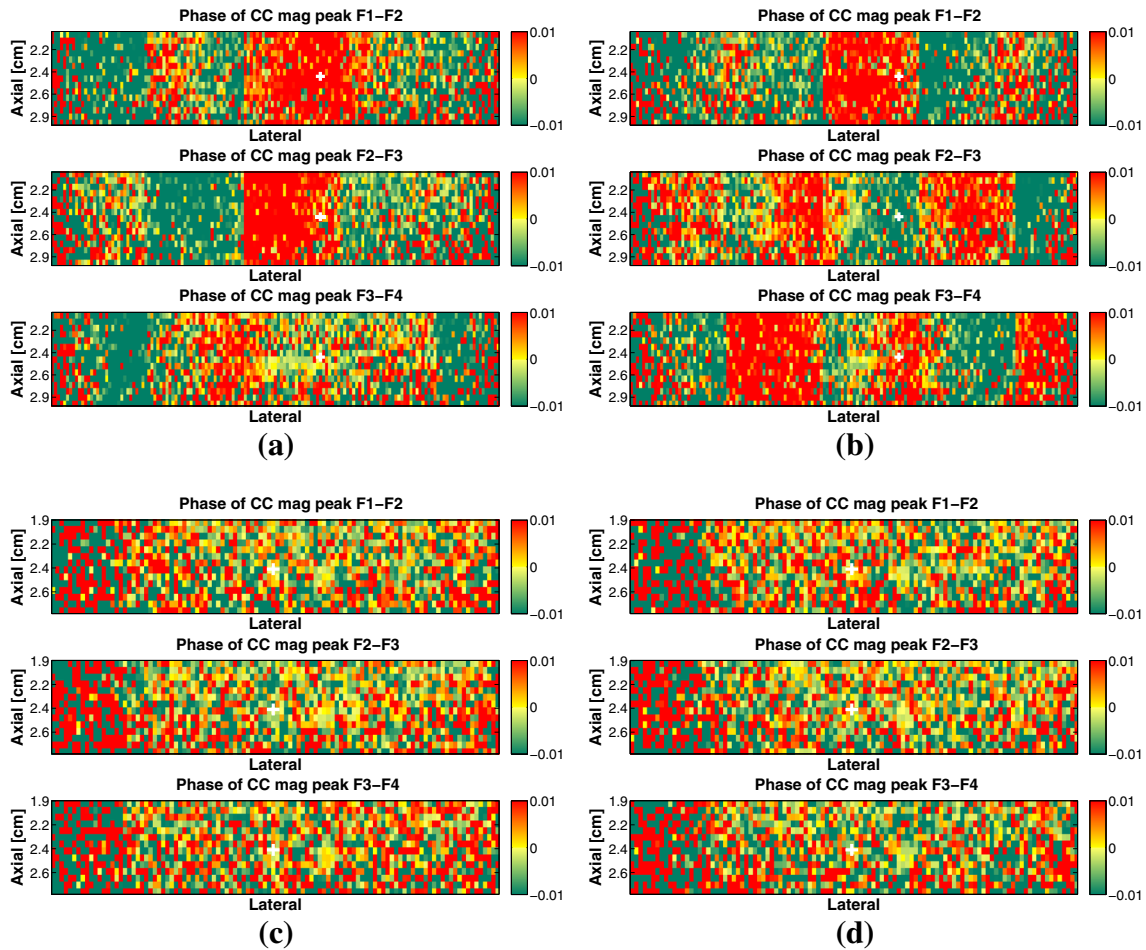Since the incident field is decomposed into the sum of plane waves, the wave propagation around MC can be described by the Helmholtz function in a viscoelastic material (Eq. 5), with dynamic viscosity μ and bulk viscosity μ_B. Benefited by the solving propagation and scattering problem in the frequency domain, the calculation in the pressure acoustics study is heavily sped up:

$$\nabla \cdot \frac{1}{\rho_c} \nabla p_t - \frac{\omega^2 p_t}{c_c^2 \rho_c} = 0 \tag{5}$$

$$\rho_c = \frac{\rho c^2}{c_c^2}, \quad c_c = c \left(1 + i\omega \frac{\frac{4\mu}{3} + \mu_B}{\rho c^2} \right)^{\frac{1}{2}}. \tag{6}$$

The discrete simulation geometry for the propagation and scattering calculation is shown in Fig. 5. Around a single MC or cluster, a close surface S_0, 1 mm away from the center, is defined to neglect the influence from the boundary layer around the particle, which is <60 μm in thickness in our scenario [26]. Six perfectly matched layers (in ocher) are used to minimize the back reflection from the tissue outer boundary interface (in blue) to mimic the acoustic scattering p_{sc} in an infinite domain (Fig. 6). In Fig. 5, the tetrahedron edge size, sufficient for the simulation accuracy, is depicted by normalization over one-sixth of the wave length, then projected on the color space.

The geometry of the mechanical model is a duplication of the phantom in the real experiment (not shown here). In addition, it is a rectangular cuboid. Four vertical walls and the bottom side of this model are constrained by a normal boundary condition: the normal displacement is zero, but they are free to move in the tangential direction. The simulation on the mechanical model is in the time domain, and the total span of one shot is equal to the length of the

Fig. 6 Scattering sound into external space by an MC particle in a soft phantom, used later to estimate primary acoustic radiation force. The *polar axis* in this figure is the sound level along with different scattering directions

Fig. 7 Color-coded expression from a homogeneous phantom with different sizes of microcalcifications. A *white cross* indicates MC location. **a**, **b** Two time frames captured with a cluster of small MCs ($\phi = 0.2$ mm); **c**, **d** two time frames with big MCs ($\phi = 1$ mm)

PRI. During a PRI, the MC (diameter ϕ of each = 0.4 mm) is driven directly by $\mathbf{F_0}$ and the tissue is pushed by F_1. Since the beam is moving iteratively among shots in steering mode, these two forces should be continuously updated and fed to the mechanical model in each beam position, as shown in Fig. 4. The estimated motion can be aggregated together time by time for our further interrogation.

In the acoustic simulation to get two ARFs ($\mathbf{F_0}$ and F_1), and the kinematic simulation on the mechanical model to get MC motions, the viscoelasticity values in Table 2 are used to define the tissue domain, while the MC is set as an elastic sphere. The density of MC is equal to 2240 kg/m^3, and the longitudinal wave velocity is 5640 m/s. The elastic modulus of MC in Anderson's paper is used here [4]. For the viscoelasticity tissue in the mechanical model, the deviatoric part in the stress tensor (S_d) is not linearly related to the deviatoric elastic strain (ε_d) by the shear modulus (G). The relationship between them follows the Kelvin–Voigt model:

$$S_d = 2(G\varepsilon_d + \eta\partial_t\varepsilon_d), \quad \eta \approx \mu \tag{7}$$

and for the viscoelastic tissue in the acoustic model, the two viscosities are coupled directly into the Helmholtz equation (such as in Eq. 5).

Results and discussion

Experiment on phantom A

After IQs are recorded, the color-coded expression is plotted to see the motion in phantoms (Fig. 7a–d). Further comparing these figures with the video clip from the scanner (V11 and V21), it could be noticed that tissue movement (reflected by the color flip in Fig. 7a and b) is closely coupled with the BFI-TS observed on video.

More evidence of motion can be provided by the box-plotting (Fig. 8) using the φ_{cc} value estimated from the IQ segments around MC (related distance in range ≈ 0.9 mm),
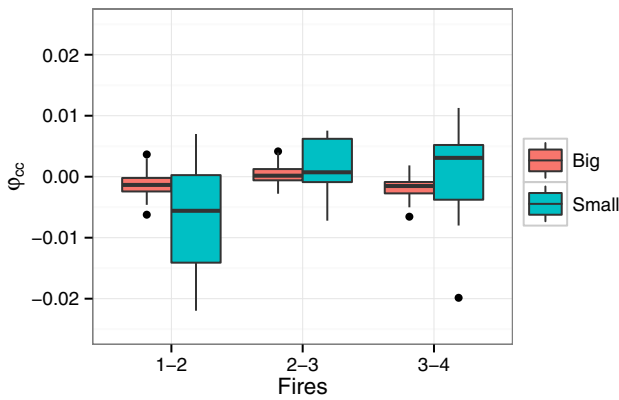
Fig. 8 Distribution of phase estimator values based on IQs retrieved from comparative test. MC size is the control factor in this experiment. Each *box* denotes 200 observations. Abscissa indicates the indexes of fires used in phase estimator calculation. For instance, 1–2 means that two related boxes are the phase estimator value coming from retrieved RFs after the first and second transmissions to a certain position. Since B-flow mode has four repetition firings, there are three columns of *boxes* in this figure. *Dots* in this figure and the next represent outliers values that lie more than $1.5 \times$ the interquartile range from either side of the box

corresponding to the different MC sizes (small/big). In addition, a small variance is shown in the bigger MC case, which indicates a smaller motion (ζ_m) or no vibration ($\omega_L = 0$). Meanwhile, the very test case also shows the same fact through a stationary bright dot in the BFI video clip, comparing a stronger twinkling sign observed in the smaller MC test.

Experiment on phantom set B

Similarly, the boxplot is shown after a two-factorial-designed test (Fig. 9), with each box related to 200 observations of φ_{cc} at different times. Besides the viscosity, the test introduces four levels of MC size as another control factor ($\phi = 0.2, 0.5, 1.0, 2.0$ mm).

In the statistical inference thereafter, the F-statistic first shows a strong significant dependence between dependent and independent variables ($p < 2.2 \times 10^{-16}$ for the three corresponding firings). Then, t test on each coefficient shows strong significant influences from tissue viscoelasticity ($p < 2 \times 10^{-16}$), but not enough certainty to claim significant influence from MC size ($p > 0.1$ in the second and third firings, $p > 0.01$ in the first firing). During this linear regression analysis, the normality of residuals and heterogeneity of variance is considered.

Observations and learning in the experiment

Through the phantom study, the viscoelasticity of tissue could now be claimed as the significant dominant factor for the twinkling sign. Moreover, it could serve as minor evidence of a mechanical motion from MC, since the viscoelasticity is coupled with parameters in a mechanical model if the latter one is used to characterize the tissue behavior under different stresses. During the experiment on phantom A, the size of the MC is found to impact the twinkling sign. While on phantom B, it is put into the
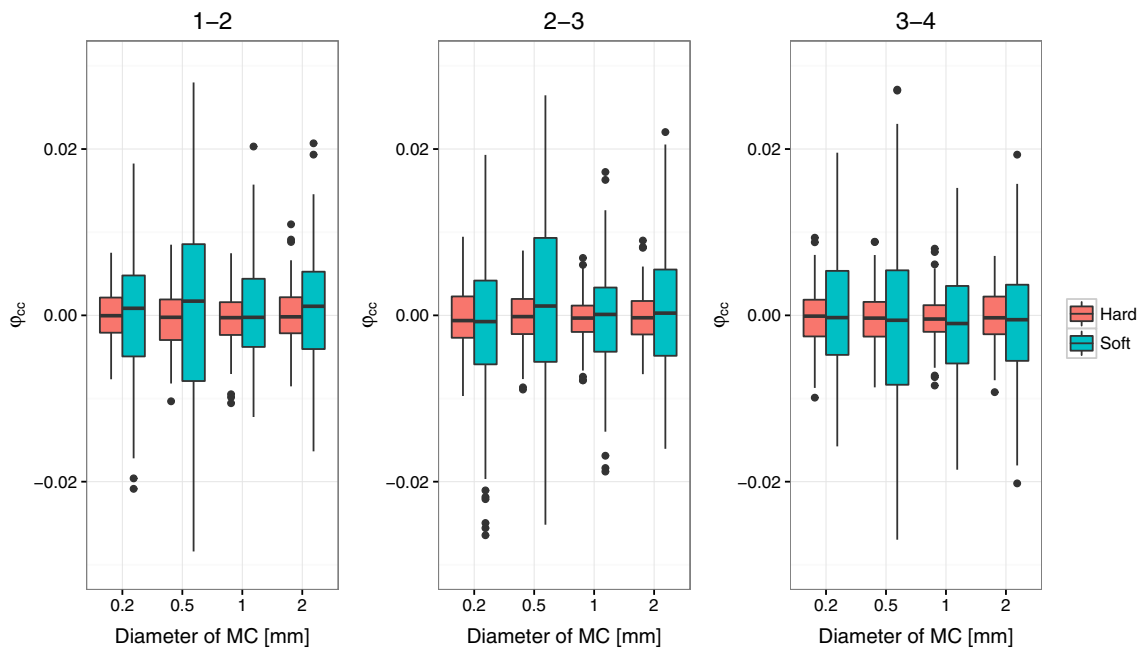
Fig. 9 Distributions of phase estimator values from a balance designed analysis. There are two factors: viscoelasticity (soft and hard as in Table 2) and sizes of the MC (0.2, 0.5, 1.0, and 2.0 in mm) in this test

regression analysis as a numerical variable to summarize the trends of the twinkling towards this factor. In addition, unfortunately, this time, the size of the MC is no longer shown as a significant one. Therefore, in the simulation validation, we try to constrain ourselves on the viscoelasticity.

Simulation to validate of the influence from the viscoelasticity

Following the steps introduced in the methodology, in the simulation, the motion of a single MC as long as the B-flow signal generated thereafter is set as our major interrogation target. After the simulation, the motion of this particle in continuous frames is compared in Figs. 10 and 11. Larger

displacement is observed on the soft phantom ($\approx 1.5 \times 10^{-8}$ m) as compared with its counterpart ($\approx 0.7 \times 10^{-8}$ m) on the hard phantom. Moreover, a larger difference in displacement between interleaved firings in the same frame, i.e., the difference between the same color peaks, is noticed too on the soft phantom. And that is known for leading to a larger B-flow signal after the coherent filtering performed on the ensemble IQ signal [7].

To cross validate the statement, the B-flow RF signal is composed based on the motion retrieved from the FEM simulation (see Figs. 10, 11). A larger shift of the peaks in continuous frames along the beam direction is observed on the soft phantom (25.5544, 25.6506, and 25.5640 mm in three simulated frames). On the counterpart, the shift is merely distinguishable in the hard phantom (25.6506,
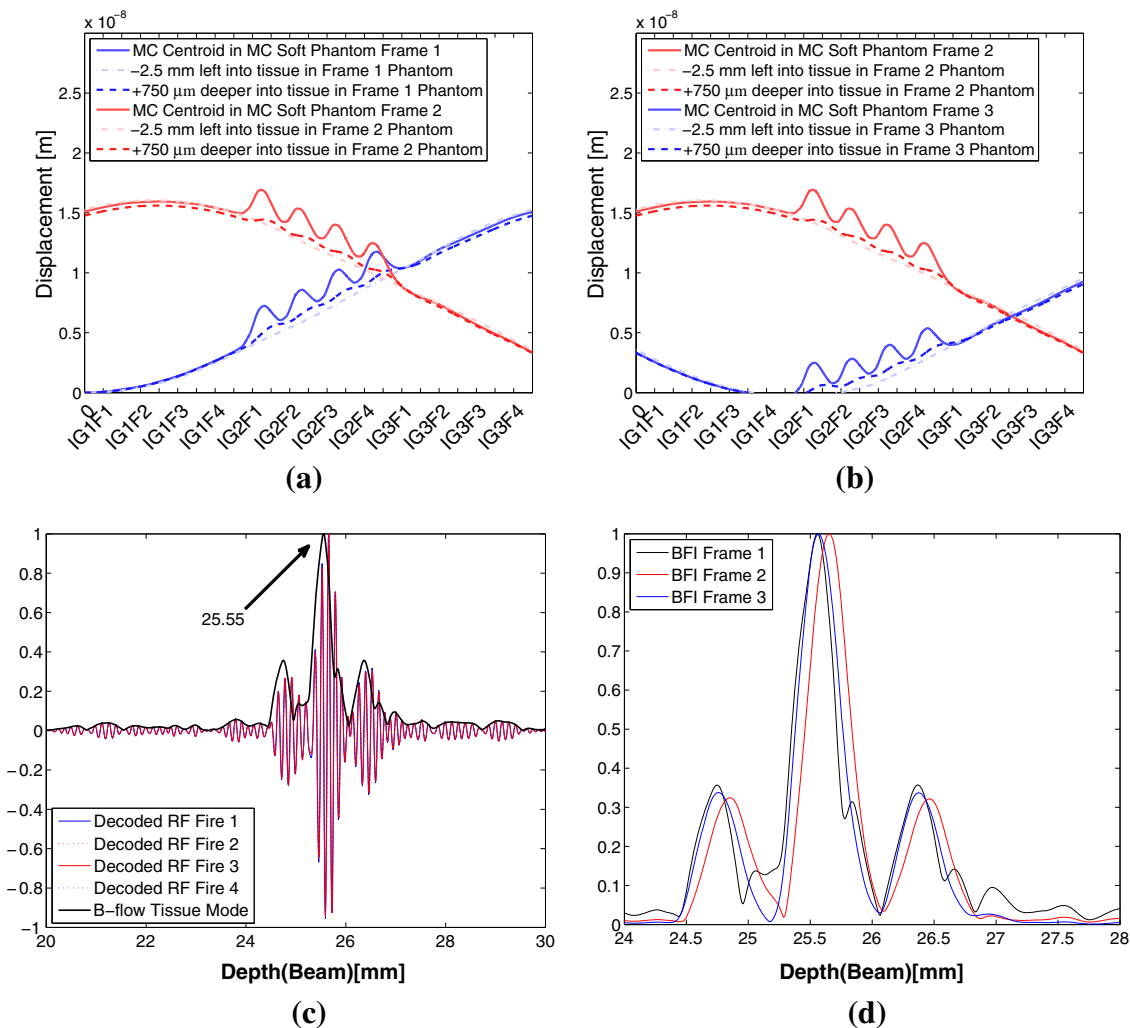
Fig. 10 Simulation results in a soft phantom. The estimated motion in the first three frames can be compared in **a** and **b**, which contain the movement of MC center (*solid line*), left tissue region 2.5 mm away from MC (*dash dot line*), and tissue region 750 μm deeper than MC center (*dash line*). The distance between the centers of two continuous interleave groups is 2.5 mm. The distance between the centers of two

continuous code bits in range axis is 750 μm. Abscissa in **a** is marked by abbreviations of interleave group and firings, e.g., IG1F1 means the first transmission in the first interleave group. In **c**, B-flow amplitude is calculated based on the estimated motion, which is the output of the coherent filtering on four decoded received RF signals. For convenience, the normalized RF amplitude is shown in **d**
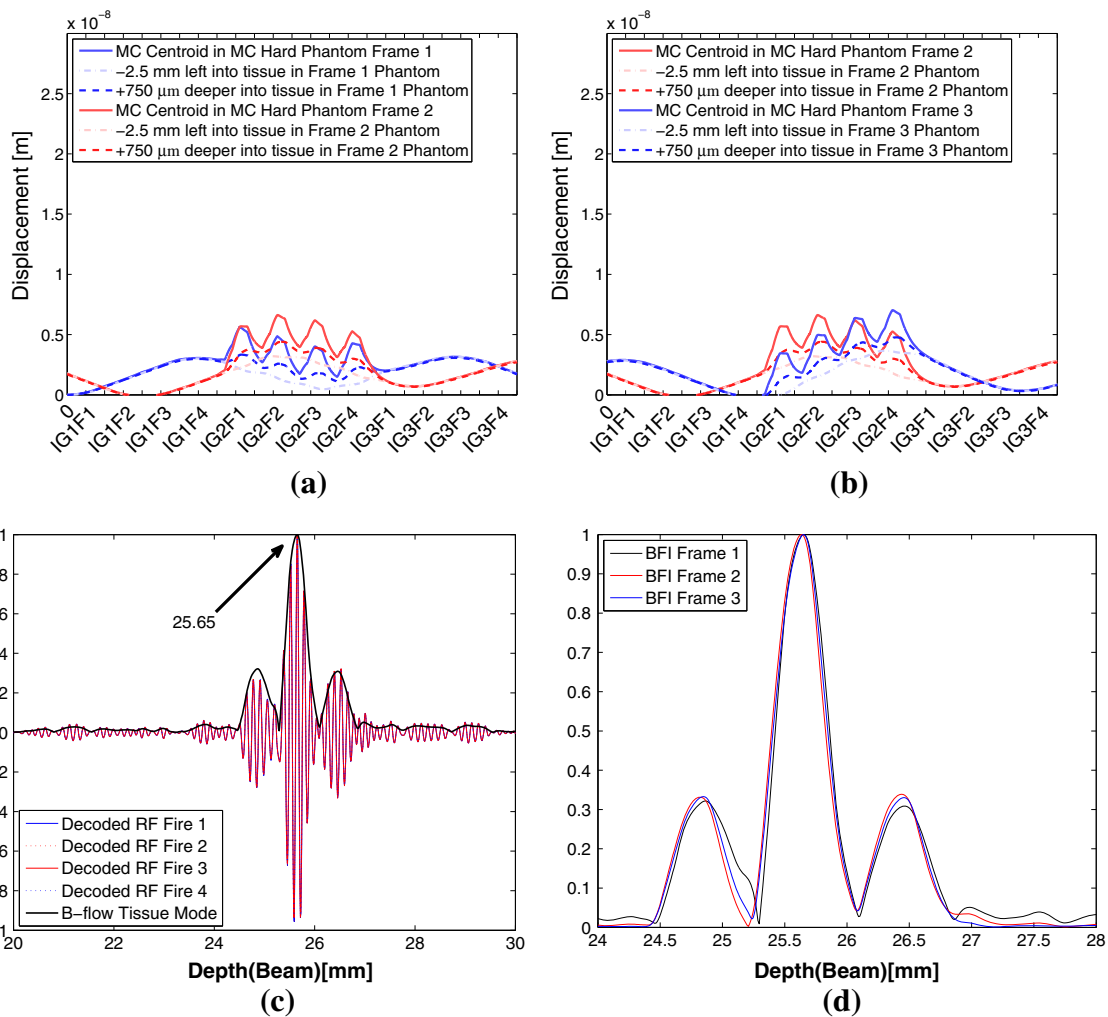
Fig. 11 Simulation result in a hard phantom

25.6314, and 25.6506 mm in three simulated frames). Thus, if the same dynamic range is operated on these signals, a larger relative shift of the bright dot reflecting the MC target should be observed on the US screen. In addition, normally, the shift of the bright dot is optically interpreted as the twinkling.

Contribution from two types of ARF

In the modeling methodology of this study, the primary ARF F_0 and the body force F_1 are both considered. A question could be raised concerning the contribution from these two kinds of ARFs. Thus, an utterly heuristic simulation is designed to investigate the motion of the MC in a soft phantom with/without the contribution of the body force F_1 (see the result in Fig. 12). The figure clearly shows that the major contribution should be the body force F_1, since it helps secure the displacement difference between interleaved firings.

Back to the normal perspective, the motion of the MC will be the triggering factor to the motion of the whole tissue specimen if the primary ARF exerted on it is the major contribution. On the other hand, the motion of the tissue will be the triggering factor if the body force generated by the steering acoustic field is the dominant factor. Thus, from the observation in this simulation, BFI-TS is interpreted as a tissue movement triggering vibration, for the purpose of separating the contributions from two kind of ARFs.

Limitation of this study

Built on the factorially designed experiment, the viscoelasticity manifests itself as the dominant factor of the twinkling sign. However, this observation needs further verification based on *in vivo* data, even though we attempted to match the acoustic characteristics of the phantoms to the characteristics of tissue.

The sand particles, acting as substitutes for the MC in the real tissue, are anchored into the phantom. Unfortunately, it is difficult to control the roughness of the
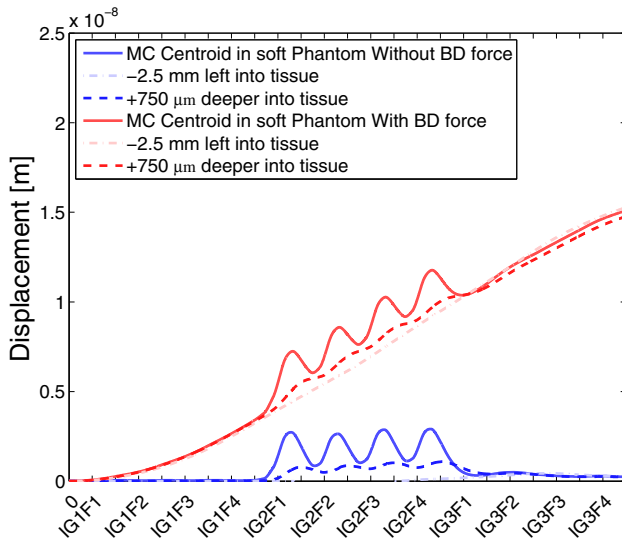
Fig. 12 Comparison of motions in a soft phantom, with or without body force from attenuation

particles' surface, which affects their reflectivity (particle size is on the order of a wavelength). The simulation presented in this study uses an ideal sphere and fluid-solid interface in calculating the scattering field. At this time, the effect of the particles' surface roughness cannot be quantitatively assessed. However, the smoothness assumption does not diminish the major finding in this study. The phantom experiment reported by Liu [10] used smooth glass beads and reported similar BFI-TS results indicating that underlying effect is the same.

In the simulation, the primary acoustic force exerted on a single MC is considered, but the secondary force responsible for the MC–MC interaction is ignored. Such an assumption is made, since the secondary force is known to connect to the morphology of the cluster [29], which needs further *a priori* anatomy information and could be different in the subjects of the ultrasonic scanning. To understand the contribution of the secondary radiation force, a comparative experiment could be performed directly in an *in vivo* test.

Conclusions

In this study, the mechanism of the BFI-TS was investigated based on the findings and hypotheses in the previous contributions [10, 13]. Fully factorially designed phantom experiments were first introduced. To analyze the retrieved data, an innovative representation of the object vibration (the variance of φ_{cc}) was deduced and used in the following statistical inference on linear regression modeling. Based on the phantom experiment and the inference result, the viscoelasticity of the tissue became our interrogation

target in the computational simulation. In the simulation, two types of ARFs, one from the particle scattering and the other from the tissue dissipation, were employed as the driving force. And cross validated by the simulation result, the soft tissue with smaller viscoelasticity led to a larger displacement of the MC. Moreover, as enlightened by the simulation, the ARF from the tissue dissipation played as critical role in generation of the twinkling sign. Based on this understanding, the BFI-TS was interpreted as a tissue movement triggering vibration of the MC particle.

Compliance with ethical standards

Ethical statements All procedures and experiments were conducted on phantoms.

Conflict of interest There are no financial or other relations that could lead to a conflict of interest.

Appendix: the motion estimator and its statistical characteristics

Suppose a signal is emitted, and two received signals are as follows [18]:

$$
\begin{aligned}
g_{r_0}(t) &= g_0(t)\cos(\omega_0 t) = \mathcal{F}^{-1}G_r(\omega) \\
g_{r_1}(t) &= g_0(t-t_1)\cos(\omega_0(t-t_1)) + n_1(t) \\
g_{r_2}(t) &= g_0(t-t_2)\cos(\omega_0(t-t_2)) + n_2(t).
\end{aligned}
\tag{8}
$$

Transforming the correlation into the Fourier domain results in Eq. 9 [18]. This equation indicates that the cross correlation between two RF data segments is a lag version of the auto correlation:

$$
\begin{aligned}
CC_{21}^r(t) &= \mathcal{F}^{-1}\left\{ G_r(\omega)e^{-j\omega\Delta t}G_r^*(\omega) \right\} + n_1^r(t)\star n_2^r(t) \\
&= CC_{11}^r(t-\Delta t) + n_1^r(t)\star n_2^r(t).
\end{aligned}
\tag{9}
$$

If the data are processed as baseband IQ complex samples, the cross correlation needs another phase term for the center frequency, as in Eq. 10, since the lag happens before demodulation:

$$
\begin{aligned}
CC_{21}^b(t) &= \mathcal{F}^{-1}\left\{ G_b(\omega)e^{-j(\omega_0+\omega_b)\Delta t}G_b^*(\omega) \right\} + n_1^b(t)\star n_2^b(t) \\
&= CC_{11}^b(t-\Delta t)e^{-j\omega_0\Delta t} + n_1^b(t)\star n_2^b(t).
\end{aligned}
\tag{10}
$$

Equation 10 reveals that the phase of CC_{21}^b is only determined by the center frequency ω_0 and delay Δt, regarding the moment when CC_{21}^b reaches its peak in magnitude. Thus, a coarse delay estimator is raised from the phase of cross correlation in that position. A similar deduction can be found in the paper by Gough [18] and Marple [19].

Let us consider that the movement of a resonating target can be decomposed into harmonic components. Each component can be formulated as in Eq. 11. ω_L is its natural frequency which usually depends on the mechanical characteristics of the system, and ϕ_0 is its random phase following a uniform distribution $\mathbb{U}(-\pi, \pi)$:

$$\zeta(t) = \zeta_m \sin(\omega_L t + \phi_0). \tag{11}$$

The resonance causes a lag on the received signal, as denoted in Eq. 12, and ΔT is the sampling rate of ensemble train. In interleave scan mode, this value is equal to the interleave group size (IGS) times the PRI of each pulse:

$$
\begin{aligned}
\Delta t &= \frac{2(\zeta(2\Delta T) - \zeta(\Delta T))}{c} \\
&= \frac{2\zeta_m}{c}\left\{ \sin(2\omega_L \Delta T + \phi_0) - \sin(\omega_L \Delta T + \phi_0) \right\} \\
&= \frac{4\zeta_m}{c}\cos\left(\frac{3\omega_L \Delta T + 2\phi_0}{2}\right)\sin\left(\frac{\omega_L \Delta T}{2}\right).
\end{aligned} \tag{12}
$$

In addition, the variance of estimator $\varphi_{cc} = \omega_0 \Delta t$ can be calculated as in Eqs. 13–16:

$$\sigma_{\varphi_{cc}}^2 = E(\varphi_{cc}^2) - E(\varphi_{cc})^2 \tag{13}$$

$$E(\varphi_{cc}) = 0 \tag{14}$$

$$E(\varphi_{cc}^2) = \frac{8}{c^2}\left(\zeta_m \omega_0 \sin\left(\frac{\omega_L \Delta T}{2}\right)\right)^2 \tag{15}$$

$$\sigma_{\varphi_{cc}}^2 = \frac{4}{c^2}(\zeta_m \omega_0)^2 (1 - \cos(\omega_L \Delta T)). \tag{16}$$

Thus, the variance of this phase estimator could reflect the resonance amplitude as long as it is compared under a constant IGS setting, i.e., a constant ΔT.

Videos are retrieved from the Logic E9 US machine, and post-processed by Avidemux [32]. During post-processing, the near-field in the US video is cropped, the color in each frame is removed, and the contrast is regulated to the same scale.

References

1. Anderson ME, Soo MS, Bentley RC, et al. The detection of breast microcalcifications with medical ultrasound. J Acoust Soc Am. 1997;101:29–39.

2. Bagnall MC, Evans AJ, Wilson AM, et al. Predicting invasion in mammographically detected microcalification. Clin Radiol. 2001;56:828–32.

3. Frates MC, Benson CB, Charboneau JW, et al. Management of thyriod nodules detected at US: society of radiologists in ultrasound consensus conference statement. Radiology. 2005;237:794–800.

4. Anderson ME, Soo MS, Trahey GE. Microcalcifications as elastic scatters under ultrasound. IEEE Trans Ultrason Ferr. 1998;45:925–34.

5. Anderson ME, Soo MS, Trahey GE. The acoustic properties of microcalcifications in the context of breast ultrasound. J Acoust Soc Am. 1998;103:1853–4.

6. Anderson ME, Soo MS, Trahey GE. In vivo breast tissue backscatter measurements with 7.5 and 10 mhz transducers. Ultrasound Med Biol. 2001;27:75–81.

7. Chiao RY. B-mode blood flow (B-flow) imaging. Ultrason Symp 2000 IEEE. 2000;2:1469–72.

8. Brunese L, Romeo A, Iorio S, et al. Thyroid B-flow twinkling sign: a new feature of papillary cancer. Eur J Endocrinol. 2008;159:447–51.

9. Brunese L, Romeo A, Iorio S, et al. A new marker for diagnosis of thyroid papillary caner. J Ultras Med. 2008;27:1187–94.

10. Liu L, Funamoto K, Ozawa K, et al. In vitro study of ultrasound radiation force-driven twinkling sign using PVA-H gel and glass beads tissue-mimicking phantom. J Med Ultras. 2013;40:197–203.

11. Rahmouni A, Bargoin R, Herment A, et al. Color Doppler twinkling artifact in hyperechoic regions. Radiology. 1996;199:269–71.

12. Kamaya A, Tuthill T, Rubin JM. Twinkling artifact on color Doppler sonography: dependence on machine parameters and underlying cause. Am J Roentgenol. 2003;180:215–22.

13. Behnam H. Modeling twinkling artifact in sonography. In: Bioninformatics and Biomedical Engineering (ICBBE), 2010 4th International Conference. 2010;2:1–4.

14. Jensen JA, Svendsen NB. Calculation of pressure fields from arbitrarily shaped, apodized, and excited ultrasound transducers. IEEE Trans Ultrason Ferr. 1992;39:262–7.

15. Shimazaki T. Ultrasonic pulse transmission method and ultrasonic diagnostic apparatus. US Patent. 2008; 7448997.

16. Lu W, Niu R, Yuan L, et al. Method to develop coded excitation for velocimetry in downhole drilling. In: Computer and Information Technology; Ubiquitous Computing and Communications; Dependable, Autonomic and Secure Computing; Pervasive Intelligence and Computing (CIT/IUCC/DASC/PICOM), 2015 IEEE International Conference. 2015;855–60.

17. Jensen JA. Artifacts in blood velocity estimation using ultrasound and cross-correlation. Med Biol Eng Comput. 1994;32:165–70.

18. Gough PT. Signal processing and correlation techniques. 2008. https://www.scribd.com/document/149011617/UIA-Correlation, http://citeseerx.ist.psu.edu/viewdoc/summary?doi=10.1.1.517.2966. Accessed 5 Nov 2003.

19. Marple JSL. Estimating group delay and phase delay via discrete-time "analytic" cross-correlation. IEEE Trans Signal Proces. 1999;47:2604–7.

20. Niu FQ, Zhu CG, Chen Y. GB/T 15261-2008:Measurement methods for acoustic properties of ultrasonically tissue-mimicking materials. Standardization Administration of China; 2008. p. 2–3.

21. Niu FQ, Zhu CG, Chen Y, Jiang SL. Technical requirements for sonoelasticity tissue-mimicking phantom (in press).

22. Feng R. Ultrasonics handbook. Nanjing: Nanjing University Publishing House; 1999. p. 101–2.

23. King LV. On the acoustic radiation pressure on spheres. Proc R Soc Lond A. 1933;147:212–40.
24. Westervelt PJ. The theory of steady forces caused by sound waves. J Acoust Soc Am. 1951;23:312–5.
25. GorKov LP. On the forces acting on a small particle in an acoustical field in an ideal fluid. Sov Phys Dokl. 1962;6:773.
26. Settnes M, Bruus H. Forces acting on a small particle in an acoustical field in a viscous fluid. Phys Rev E. 2012;85:016327.
27. Sapozhnikov OA, Bailey MR. Radiation force of an arbitrary acoustic beam on an elastic sphere in a fluid. J Acoust Soc Am. 2013;133:661–76.
28. Muller PB, Bruus H. Numerical study of thermoviscous effects in ultrasound-induced acoustic streaming in microchannels. Phys Rev E. 2014;90:043016.
29. Doinikov AA. Acoustic radiation forces: classical theory and recent advances. Recent Res Devel Acoust. 2003;661:39–67.
30. Palmeri ML, Sharma AC, Bouchard RR, et al. A finite-element method model of soft tissue response to impulsive acoustic radiation force. IEEE Trans Ultrason Ferr. 2005;52:1699–712.
31. Nightingale K. Acoustic radiation force impulse (ARFI) imaging: a review. Curr Med Imaging Rev. 2011;7:328.
32. Fixounet. Avidemux home site. 2016. https://github.com/mean00/avidemux2, https://sourceforge.net/projects/avidemux/. Accessed 17 Sep 2016.